Full Length Article

Mass calibration of Rosetta's ROSINA/DFMS mass spectrometer

J. De Keyser [a,b,*], F. Dhooghe [a], K. Altwegg [c], M. Rubin [c], N. Hänni [c], S.A. Fuselier [d], J.-J. Berthelier [e], E. Neefs [f]

[a] *Space Physics Division, Royal Belgian Institute for Space Aeronomy, Ringlaan 3, B-1180 Brussels, Belgium*
[b] *Center for Plasma Astrophysics, Katholieke Universiteit Leuven, Celestijnenlaan 200B, B-3001 Heverlee, Belgium*
[c] *Physikalisches Institut, University of Bern, Sidlerstr. 5, CH-3012 Bern, Switzerland*
[d] *Department of Space Science, Southwest Research Institute, 6220 Culebra Road, San Antonio, TX 78228, USA*
[e] *Laboratoire Atmosphères, Milieux, Observations Spatiales, Institut Pierre Simon Laplace, CNRS, Université Pierre et Marie Curie, 4 Avenue de Neptune, F-94100 Saint-Maur, France*
[f] *Engineering Division, Royal Belgian Institute for Space Aeronomy, Ringlaan 3, B-1180 Brussels, Belgium*

ARTICLE INFO

ABSTRACT

The Double Focusing Mass Spectrometer (DFMS) onboard the Rosetta spacecraft employs an electrostatic and a magnet sector for energy and mass discrimination, resulting in a high mass resolution. A built-in feedback loop uses the measured magnet temperature to compensate for the temperature dependence of the magnet's field strength. Still, large onboard temperature variations and other effects cause any given mass peak to move over a range of 30 pixels or more on the detector during the mission. The present paper discusses the various factors that contribute to the time variations in the mass calibration relation. A technique is developed to evaluate and correct for these factors. A mass calibration relation that is valid for the DFMS neutral high mass resolution mode measurements throughout the entire mission for the mass range $m/z =13–69$ is established and its accuracy is evaluated. The 1σ precision turns out to be less than a single pixel, which is excellent as full peak width at half height is about 12 pixels. The proposed approach provides an a posteriori mass calibration and is useful for all magnet-based mass spectrometers where experimental mass calibration by comparison to reference species, temperature stabilization, and/or electrostatic compensation, are not possible or fail to deliver a mass scale precision that is comparable to the mass resolution of the instrument.

1. Introduction

The Rosetta spacecraft of the European Space Agency (ESA) visited comet 67P/Churyumov-Gerasimenko in 2014–2016. Its instrument suite included ROSINA (Rosetta Orbiter Spectrometer for Ion and Neutral Analysis), a mass spectrometry package for analyzing the atmosphere of the comet [1]. Since the comet atmosphere is formed by sublimation of volatile constituents [e.g., 2,3] or by sputtering of surface material [4], such measurements provide insight into comet nucleus composition.

The present paper deals with the Double Focusing Mass Spectrometer (DFMS), a high mass resolution instrument that is part of ROSINA [1]. DFMS can sample either the ambient ions (ion modes) or the neutral gas (neutral modes), by using an electric potential barrier to block the ions from entering the instrument. Only the instrument's neutral modes without post-acceleration (no additional electrostatic potential difference between the mass analyser exit and the detector) are considered here (mass-over-charge 13–69). A schematic diagram of

the instrument is presented in Fig. 1. Neutral cometary gas enters DFMS through a $20° \times 20°$ field-of-view aperture. A fraction of the molecules is ionized or broken up into neutral and/or charged fragments in the ion source by electron ionization, with the electrons being emitted by a filament and accelerated through a 45 V potential. The resulting ions are extracted from the source through a slit and are accelerated by a voltage V_{accel} that is chosen as a function of the mass. The analyser has a Nier–Johnson geometry [5] in which the charged particle beam is deflected over 90° by an electrostatic energy analyser, followed by a deflection over 60° by a permanent magnet. Additional optical elements in the beam allow to select low or high mass resolution mode (LR/HR). These include electrostatic fields used to switch between the LR and HR slits, as well as electromagnets for the zoom optics immediately behind the magnetic sector that are used in HR mode to increase the beam dispersion. Finally there is also the possibility to apply an electric potential between the exit of the zoom optics and the detector to provide "post-acceleration" of the ions to enhance
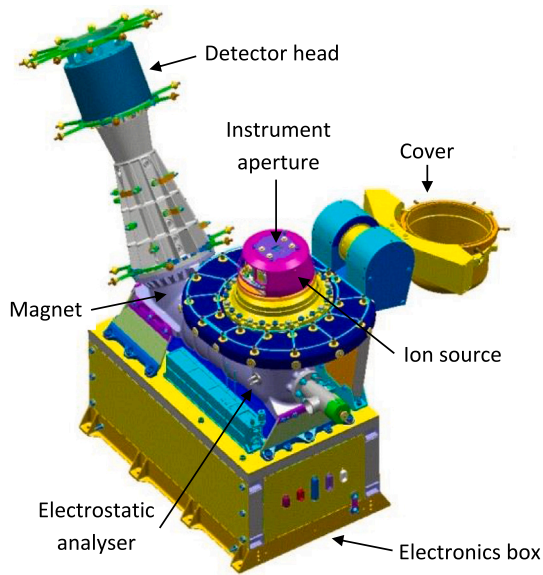
Fig. 1. A schematic overview of the DFMS mass spectrometer.

the instrument sensitivity, which is applied only for higher masses. The resulting ion beam is usually recorded by a position-sensitive combination of a microchannel plate (MCP) with a linear CCD (the Linear Electron Detector Array or LEDA chip). The MCP consists of two layers with narrow channels in chevron configuration [6]. Ions incident on the MCP channels create secondary electrons, which are accelerated by a static high voltage between the front and back ends of the MCP; this voltage determines the "gain" of the detector. As a result, an electron avalanche exits the MCP and impacts the CCD. Upon impact, these electrons can produce secondaries as well. The whole process of ion impact and secondary electron generation plays an important role in understanding how the detector ages and how one can correct for this aging [7]. At maximum gain, 1 incident ion produces about 10^5 electrons. The LEDA chip has two parallel rows of charge collecting anodes, channels A and B [6,8]. Each anode pixel is able to hold up to 5×10^7 electrons, and is read out every 6.55 ms. The CCD output is digitized with 12 bits by an analog-to-digital converter providing a number of electron counts per pixel (1 ADC count is equivalent to 13 000 electrons), which can be translated into a number of detected ions by accounting for the secondary electron yield of the ions and the MCP characteristics [9]. A spectrum is built from 3000 accumulation steps for a total of 19.66 s. The MCP/LEDA combination provides two redundant 512-pixel mass spectra in an interval centered on the commanded mass-over-charge value (channel A and B). The mass resolution is around $m/\Delta m = 3000$ in HR mode, where Δm is the full width at 1% of the mass peak height at $m/z = 28$ [1,7,10]. This high mass resolution has allowed the instrument to make key scientific discoveries [e.g. 2–4,11,12].

Basis for a reliable exploitation of DFMS data is the ability to provide an accurate mass scale. DFMS was equipped with a gas calibration unit (GCU) holding a reference gas mixture containing CO_2 and the noble gases Ne and Xe, with terrestrial isotope composition [1]. This provides exact mass reference points to facilitate mass calibration. However, the GCU failed before arriving at the comet. Often a priori knowledge about comet composition allows to identify a few species in a spectrum, from which a mass scale can be derived. For instance, spacecraft outgassing during cruise towards the comet offered some mass calibration reference points [13]. But this is a manual and time-consuming process and may not even work if some species are only intermittently present above the noise level.

Mass calibration ideally consists of establishing a relation that associates a value of m/z with each pixel p of the LEDA array when

the instrument is operated at a commanded mass-over-charge m_c/z. Different calibration relations must be established for low and high resolution modes as well as for high sensitivity modes involving post-acceleration, since these modes use different settings of the electric potentials in the ion optics. The analysis presented here is limited to the neutral high resolution MCP/LEDA modes, the modes most often used in space. Hypersensitive modes and the range $m_c/z > 69$, which both use post-acceleration, are not considered. The empirically established mass scale for a given spectrum for these neutral HR modes is

$$m/z = (m_c/z) \, e^{(p-p_0) \, \frac{x}{ZF \, d}} \tag{1}$$

with $p_0 = 256.5$ pixel at the center of the detector, $x = 25$ μm the distance between adjacent pixel centers, $d = 127\,000$ μm the mass dispersion, and $ZF = 6.4$ the dimensionless HR zoom factor. The instrument is designed so that the commanded mass-over-charge corresponds to the center of the detector, $m(p_0)/z \equiv m_c/z$. Alternatively, this can be expressed as

$$p = p_0 + \alpha \, \log \frac{m/z}{m_c/z} \tag{2}$$

with a dispersion factor $\alpha = \frac{ZF \, d}{x} = 32\,512$ pixel.

For reasons that will be detailed in Section 2, this mass calibration relation is an idealization. In Section 3 a methodology is presented to compute a mass calibration relation that is valid for the entire duration of Rosetta's comet escort phase. Section 4 presents the mass calibration relation that results from this approach. The physical interpretation and the quality of the result are discussed in detail. The paper concludes with a summary and indicates the utility of this mass calibration.

2. Instrument behavior

This section introduces the data set used and discusses the various parameters that affect the mass calibration.

2.1. Data set

The analysis presented here uses DFMS HR neutral measurements obtained near the comet, between August 2014 and September 2016. In a first step, an automated script determines for each spectrum the positions and peak counts for the 10 highest peaks, both on channel A and B (not all of these peaks are used; some might be spurious features or noise). In doing so, some spectra with small data issues have been repaired, while spectra with more serious problems were discarded. Peak positions have been determined after first interpolating the data down to 0.1 pixel precision using cubic splines. The smooth shape of the peaks allows to locate their positions consistently with a precision of 0.2 pixel or better. DFMS mass peaks consist of two Gaussians centered at the same position, with the second Gaussian being broader and only at about 10% of the total peak intensity, denoted here with N, the number of ions detected during the 19.66 s data accumulation time [9]. Due to the Poisson nature of the random incidence of ions on the detector, this double Gaussian peak shape is obtained only when a sufficient number of ions is detected; for lower ion counts the resulting peaks can be deformed and tend to have an off-nominal position because of the low statistics [9]. Peak position is correct up to 1 pixel when at least 100 ions are counted. The peak position error can thus be estimated by

$$\delta p = \frac{100}{N} + 0.2 \text{ pixel}. \tag{3}$$

In a second step, for each commanded mass-over-charge, the species listed in Table 1 are associated with the corresponding peaks. This is achieved as follows.

For a limited set of commanded mass-over-charge ($m_c/z = 20$, 24, 30, 32, 44), a spectrum-by-spectrum match of the masses in Table 1 with the 10 identified peaks yields an unambiguous identification. The result of this step is an assessment of how the peak position differs from the

Table 1

Species used in the analysis: m_c/z is commanded mass-over-charge, m/z the ion mass-over-charge, Δp_{bs} the beam shift, and α the dispersion factor.

| m_c/z	m/z	ion	Δp_{bs} [pixel]	α [pixel]
13	13.0073	$^{12}CH^+$	48.0	26 000
14	13.9969	$^{12}C^{16}O^{++}$	51.2	26 800
	14.0025	$^{14}N^+$		
	14.0151	$^{12}CH_2^+$		
15	15.0104	$^{14}NH^+$	56.5	28 800
	15.0229	$^{12}CH_3^+$		
16	15.9944	$^{16}O^+$	60.2	31 000
17	17.0024	$^{16}OH^+$	61.0	32 000
18	18.0100	$H_2^{16}O^+$	61.5	32 000
19	19.0064	$H^{18}O^+$	62.8	30 000
	19.0178	$HD^{16}O^+, H_3^{16}O^+$		
20	20.0143	$H_2^{18}O^+$	62.5	32 000
21	21.0215	$HD^{18}O^+, H_3^{18}O^+$	62.5	32000
22	21.9944	$^{12}C^{16}O_2^{++}$	63.0	32 250
23	22.9892	$^{23}Na^+$	62.5	32 250
	22.9965	$^{12}C^{16}O^{18}O^{++}$		
24	23.9994	$^{12}C_2^+$	62.5	32 250
25	25.0073	$^{12}C_2H^+$	62.5	32 250
26	26.0025	$^{12}C_2^{14}N^+$	62.8	32 300
	26.0151	$^{12}C_2H_2^+$		
27	27.0104	$H^{12}C^{14}N^+$	62.8	32 300
	27.0229	$^{12}C_2H_3^+$		
28	27.9944	$^{12}C^{16}O^+$	62.9	32 400
	28.0307	$^{12}C_2H_4^+$		
29	29.0024	$^{12}CH^{16}O^+$	62.9	32 400
	29.0386	$^{12}C_2H_5^+$		
30	29.9974	$^{14}N^{16}O^+$	63.0	32 400
	30.0100	$^{12}CH_2^{16}O^+$		
	30.0464	$^{12}C_2H_6^+$		
31	31.0178	$^{12}CH_3^{16}O^+$	63.0	32 400
32	31.9715	$^{32}S^+$	63.0	32 400
	31.9893	$^{16}O_2^+$		
	32.0257	$^{12}CH_4^{16}O^+$		
33	32.9793	$H^{32}S^+$	63.0	32 400
34	33.9673	$^{34}S^+$	63.0	32 200
	33.9872	$H_2^{32}S^+$		
35	34.9751	$H^{34}S^+$	63.2	33 000
36	35.9830	$H_2^{34}S^+$	63.3	32 600
	35.9994	$^{12}C_3^+$		
37	36.9654	$^{37}Cl^+$	63.4	32 400
	37.0073	$^{12}C_3H^+$		
38	37.9715	$^{12}C^{32}S_2^{++}$	63.4	32 400
	38.0025	$^{12}C_2^{14}N^+$		
	38.0151	$^{12}C_3H_2^+$		
39	38.9694	$^{12}C^{32}S^{34}S^{++}$	63.4	32 400
	39.0229	$^{12}C_3H_3^+$		
40	39.9944	$^{12}C_2^{16}O^+$	63.4	32 400
	40.0182	$^{12}C_2H_2^{14}N^+$		
	40.0307	$^{12}C_3H_4^+$		
41	41.0386	$^{12}C_3H_5^+$	63.4	32 400
42	42.0100	$^{12}C_2H_2^{16}O^+$	63.4	32 400
	42.0464	$^{12}C_3H_6^+$		
43	43.0178	$^{12}C_2H_3^{16}O^+$	63.4	32 350
	43.0542	$^{12}C_3H_7^+$		
44	43.9893	$^{12}C^{16}O_2^+$	63.4	32 350
45	45.0335	$^{12}C_2H_5^{16}O^+$	63.5	32 300
46	46.0413	$^{12}C_2H_6^{16}O^+$	63.5	32 300
47	46.9950	$^{12}CH_3^{32}S^+$	63.5	32 250
48	47.9664	$^{32}S^{16}O^+$	63.5	32 250
	48.0028	$^{12}CH_4^{32}S^+$		
49	49.0106	$^{12}CH_5^{32}S^+$	63.5	32 200
50	49.9622	$^{34}S^{16}O^+$	63.5	32 200
	50.0151	$^{12}C_4H_2^+$		
51	51.0229	$^{12}C_4H_3^+$	63.5	32 150
52	52.0307	$^{12}C_4H_4^+$	63.5	32 150
53	53.0386	$^{12}C_4H_5^+$	63.4	32 100
54	54.0464	$^{12}C_4H_6^+$	63.3	32 100
55	55.0542	$^{12}C_4H_7^+$	63.2	32 050
56	56.0621	$^{12}C_4H_8^+$	63.2	32 050
57	57.0699	$^{12}C_4H_9^+$	63.2	32 000
58	58.0413	$^{12}C_3H_6^{16}O^+$	63.1	32 000
	58.0777	$^{12}C_4H_{10}^+$		
59	59.0491	$^{12}C_3H_7^{16}O^+$	63.0	32 000
60	59.9664	$^{16}O^{12}C^{32}S^+$	62.8	32 500
	60.0206	$^{12}C_2H_4^{16}O_2^+$		
61	61.0284	$^{12}C_2H_5^{16}O_2^+$	62.6	32 000
62	61.9622	$^{16}O^{12}C^{34}S^+$	62.4	32 000
63	63.0229	$^{12}C_5H_3^+$	62.3	32 000
64	63.9614	$^{32}S^{16}O_2^+$	62.2	32 000
65	65.0386	$^{12}C_5H_5^+$	62.2	32 000
66	65.9571	$^{34}S^{16}O_2^+$	62.2	32 000
67	67.0542	$^{12}C_5H_7^+$	62.2	32 000
68	68.0621	$^{12}C_5H_8^+$	62.2	32 000
69	69.0699	$^{12}C_5H_9^+$	62.2	32 000

expected one as a function of time. This is then exploited to facilitate and accelerate the identification for all other peaks listed in Table 1. An ad hoc procedure is followed for $m_c/z = 16, 17, 18$, for which V_{accel} was not stable, often leading to deformed or double peaks [10]; for these m_c/z only data from the later part of the mission were used. The fragments in Table 1 have been chosen because they are the most abundant ones, whose positions are well-defined, while avoiding (a) fragments that are only intermittently present, (b) broad unresolved peaks due to multiple fragments with very similar masses, (c) situations where fragments only produce a shoulder (not a local maximum) on the flank of the peak of a more abundant fragment. The selection is made in such a way that mistakes by the peak identification algorithm are minimized. Possible misinterpretations can be identified when the peak position difference between both channels is too large (> 10 pixels) or when the deviation from the initial peak position time variation is too large (> 3 standard deviations from the running average). At least one useful peak has been identified for each commanded mass-over-charge between 13 and 69. Only peak identifications have been used for which there are at least two ion counts per spectrum. We refrain from including ions with lower abundances because this increases the computational cost without constraining the result of the analysis very much.

In this way, one obtains for each spectrum its time t, the pixel positions p_A and p_B of the peaks on channel A and B, the peak intensities N_A and N_B, i.e., the number of ions incident on the MCP/LEDA during the 19.66 s acquisition time for each spectrum, and the peak position uncertainties δp_A and δp_B. From the instrument housekeeping data also a number of instrument temperatures are obtained. The corresponding heliocentric distance R and the solar aspect angle ψ between the spacecraft–Sun direction and the DFMS look direction are computed from the SPICE kernels.

Fig. 2 offers an overview of the data acquired for $m_c/z = 32$, good for about 14 200 spectra. Heliocentric distance varies between $R = 3.6$ au upon comet approach down to 1.24 au at perihelion in August 2015 and back out until the end of mission near 3.8 au (Fig. 2a). The solar aspect angle ψ (Fig. 2b) is never close to zero since pointing the observation deck toward the Sun could harm the instruments. Rosetta often circled the comet in terminator orbits, for which $\psi \approx 90°$. Values of $\psi > 90°$ are associated with the gradual approach to the comet from the sunward side (2014/08–2014/10), with flyby trajectories (2015/02–2015/03), and with Rosetta's time spent well ahead of the comet near perihelion (2015/09–2015/11) and in the months following a safe mode (2015/04–2015/06) due to star tracker problems caused by dust particles (safe mode data gap during 2015/03/28–2015/04/10). Deviations in ψ are also observed during the Rosetta manoeuvres for the Philae lander delivery (around 2014/11/12).

Let illumination function f_{illum} represent the solar flux reaching DFMS (Fig. 2c). The effective area of DFMS exposed to the Sun can
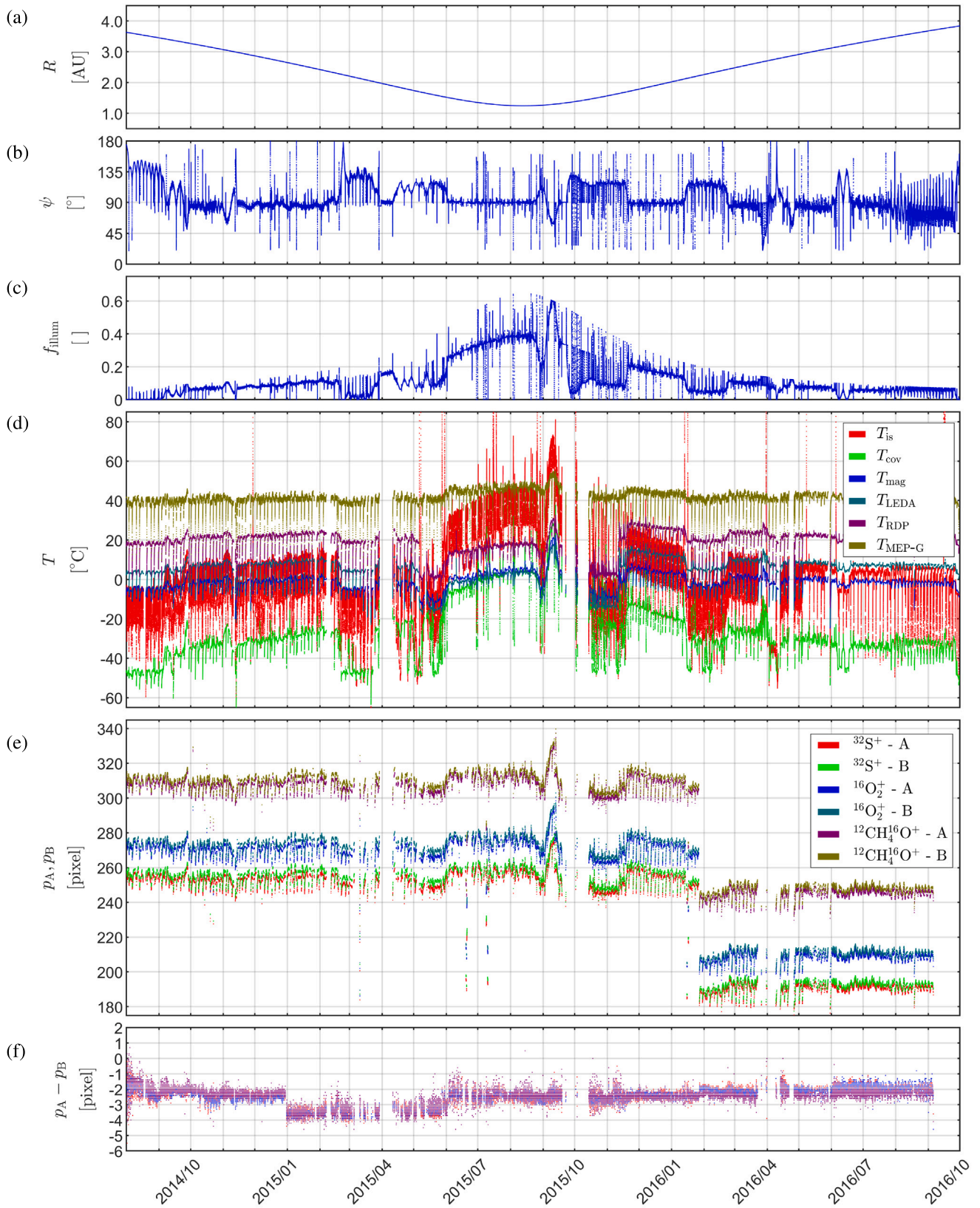
Fig. 2. An overview of DFMS data used in this study: (a) distance from the Sun R, (b) solar aspect angle ψ, (c) the illuminated fraction of DFMS f_{illum}, (d) various DFMS temperature sensor readings (see text), (e) pixel positions p_A and p_B of the 3 peaks in the $m_c/z = 32$ neutral mode HR spectra for both MCP/LEDA channels, and (f) their pixel difference $p_A - p_B$. See main text for more explanation.
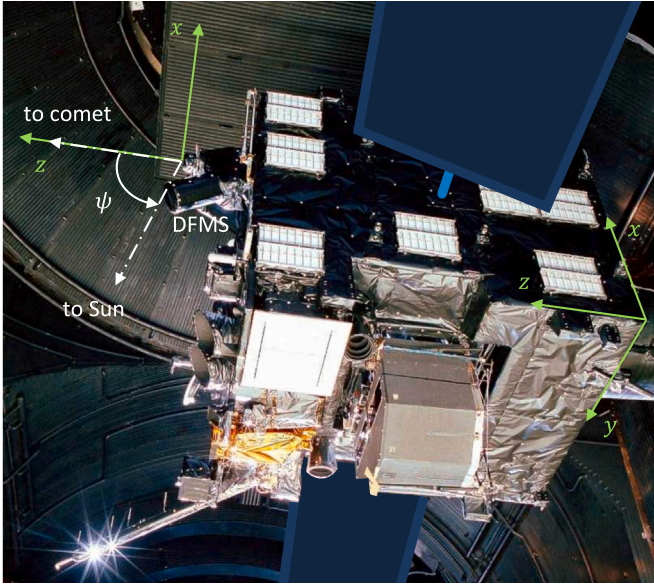
Fig. 3. Illumination of DFMS: The observation deck points toward the comet (z axis), the solar panels (along the y axis) toward the Sun, in a geometry defined by the solar aspect angle ψ. The photograph shows Rosetta during vibration testing (©ESA/Anneke Le Floc'h); solar panels are drawn on top.
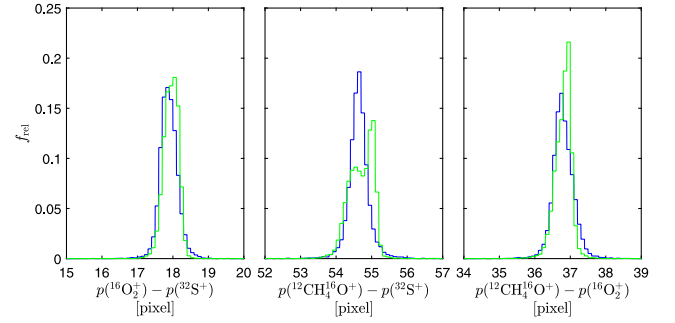

Fig. 4. Probability distributions of the differences in position of the 3 peaks in the $m_c/z = 32$ mass spectra (blue for channel A, green for channel B).

be approximated by

$$A_{exp} = \begin{cases} A_{exp,0}, & 0° \leq \psi < 60°, \\ A_{exp,0}(135 - \psi)/75, & 60° \leq \psi < 135°, \\ 0, & 135° \leq \psi \leq 180°, \end{cases} \quad (4)$$

which assumes that DFMS is fully illuminated when the Sun is $> 30°$ above the observation deck, that DFMS is in darkness when the Sun is $> 45°$ below the deck, with a linear variation in between (see Fig. 3). The solar flux reaching DFMS then is

$$f_{illum}(\psi) = \frac{A_{exp}(\psi)}{R^2 A_{exp,0}}, \quad (5)$$

with the normalization $f_{illum}(0°) = 1$ at $R = 1$ au.

Fig. 2d shows the temperature readings from a few DFMS temperature sensors (precision $0.1\,°C$). A first group of temperatures are those measured in the electronics box (only main electronics pack sensor T_{MEP-G} is shown). The power dissipation in the electronics box is fairly constant. As the box is well encapsulated below the DFMS analyzer section, the temperatures are relatively high and show little variability. However, as the electronics box is mounted to the observation deck (aluminum honeycomb) with a weak thermal coupling to the spacecraft structure, these temperatures drop significantly when DFMS is shut down because of high voltage electric discharge risks due to thruster exhaust during pre-planned momentum wheel off-loadings and orbital correction maneuvers. A second group of temperature sensors is located in the detector head. Sticking out above the observation deck and far from the electronics box, the temperatures are lower there, despite being covered by multi-layer insulation. The temperature near the MCP/LEDA detector (T_{LEDA}) is lower than that of the Remote Detector Pack (RDP) electronics (T_{RDP}) located behind the detector, where heat is dissipated. The detector head was kept from becoming too cold by having the RDP heaters ON whenever DFMS is powered. The non-operational heater in the detector head was continuously ON when Rosetta was far from the Sun. It was switched OFF on 6 May 2015, resulting in a T_{LEDA} drop of $\sim18\,°C$, and back ON on 11 November 2015, with a corresponding T_{LEDA} increase. A similar signature is present for T_{RDP}. A third group of temperature sensors are those located near the instrument aperture (T_{cov} near the cover motor, T_{is} in the ion source). The cover motor was never activated during the comet encounter. As the cover motor temperature sensor is far from any source of dissipation, it has the lowest temperatures, down to $-50\,°C$. The temperature in the ion source is similar to that of the cover motor when DFMS is shut down, but once the instrument is powered ON, the dissipation by the filament of the ion source leads to a temperature increase of about $45\,°C$. Finally, there is the temperature measured near the magnet (T_{mag}), which fluctuates around $0\,°C$, somewhere in between the temperatures in the main electronics box and in the detector head. Short-term variability in the DFMS temperatures is due to the regular instrument shutdowns, leading to recurrent temperature drops; upon instrument restart it takes DFMS a few hours to recover. Long-term time variations in the DFMS temperatures are due to changes in illumination. The correlation between f_{illum} and T_{cov} (far from any dissipation and thus controlled by illumination only) is visually evident from Fig. 2c and d.

Fig. 2e shows the peak positions of the three main peaks at $m_c/z = 32$. The peak positions p_A and p_B recorded by channel A and B are slightly different, so that there are two slightly shifted curves for each mass peak. The peak positions are seen to move collectively and one can visually notice that these motions are related to the temperature variations. In early 2016 a "beam shift" was implemented by systematically reducing the acceleration voltage. The goal was to displace the commanded mass-over-charge towards a less used part of the MCP/LEDA detector that had not yet degraded so much, in order to improve the sensitivity. This beam shift amounts to ~63 pixels at $m_c/z = 32$. In general, the shifted peaks are found at

$$\tilde{p}_{A,B} = p_{A,B} + \Delta p_{bs}(m_c/z) \quad (6)$$

where $\Delta p_{bs}(m_c/z)$ is determined a priori by comparing the average peak positions immediately before and after the shift (see Table 1). For the remainder of this paper, it is assumed that the beam shift has been applied.

The ion beam produces an image of the entrance slit on the detector. Ideally, this image should be perpendicular to the LEDA rows, but in reality there is some misalignment [7]. The resulting difference $\Delta p_{AB} = p_A - p_B$ is given in Fig. 2f. Notice that the beam shift is not visible in these curves as both p_A and p_B shift by the same amount. The differences for the three peaks are plotted together and appear to be essentially the same. The difference varies mostly between -1 and -4 pixels. There is no evident variability with temperature. Sometimes Δp_{AB} changes rather abruptly. The Δp_{AB} values spread over a range of ~0.6 pixels, consistent with the random error of 0.2 pixels on p_A and p_B and confirming the appropriateness of the peak determination procedure. Fig. 4 shows that the relative distributions of the differences between the positions of the three peaks remain within ±0.3 pixels from their average values, for each channel, again confirming that the peak position data set is accurate to 0.2 pixels and validating the use of sub-pixel precision.
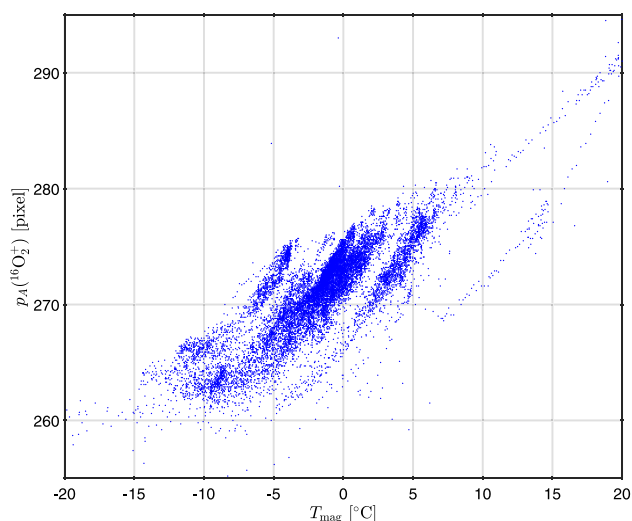
Fig. 5. Correlation between the position of $^{16}O_2^+$ in the $m_c/z = 32$ spectra (channel A after beam shift correction) and the magnet temperature T_{mag}.

2.2. Parameters affecting mass calibration

The actual mass calibration relation is more complicated than suggested by Eq. (1). Any non-ideal behavior in the ion optics (acceleration behind the source slit, deflection in the electrostatic analyzer and the magnet, dispersion in the zoom optics) modifies the relation. Moreover, the physical laws governing a mass spectrometer are continuous, while the control laws for operating the instrument work via the setting of electric potentials, limited to a discrete set of values. Therefore, although the mass calibration relation can theoretically be described by continuous laws, in practice the relation is a discrete one.

2.3. Magnetic fields

The magnet strength depends on its temperature T_{mag}. This dependence has been established prior to flight as [14]

$$B = 0.3550[T] - 1.7262 \times 10^{-4}[T/°C](T_{mag} - 22.0)[°C].$$

The nuclear spin ordering in the Sm-Co magnet alloy and in the Fe-Co yoke and pole pieces is perturbed as temperature increases, reducing magnet strength and shifting the mass peaks. A weaker field implies a lower Lorentz force and thus less bending and a shift towards higher pixel position (higher mass) on the detector.

This effect is rather dramatic. For instance, as the temperature increases from 0 to 22 °C, the field strength changes by a factor 0.9893 from 0.3550 to 0.3512 T, corresponding to a displacement of the mass scale by $f = 1.07\%$ (the displacement is inversely proportional to B) or $\alpha f = 348$ pixels. A mass peak located at the center of the detector at 0 °C thus would be off the detector at 22 °C. DFMS therefore features a feedback system that adapts V_{accel} based on the continuous measurement of T_{mag}. This feedback loop is meant to remove the effect of T_{mag} from the mass calibration relation. Unfortunately, a temperature dependence remains present. This is evident in Fig. 5, which correlates the position of the $^{16}O_2^+$ peak in the $m/z = 32$ spectra from channel A (after correcting for the beam shift) to T_{mag}. There is a positive correlation at short time scales (variations related to instrument shutdown and cold restart). Hence, the uncertainty in temperature correlates with an uncertainty in pixel position, $\delta p_T \propto \delta T_{mag}$. The temperature discretization is $2\delta T_{discr} = 0.1$ °C, while the actual measurement accuracy is estimated to be $\delta T_{meas} = 0.15$ °C at 3σ-level, leading to $\delta T_{mag} = (\delta T_{discr}^2 + \delta T_{meas}^2)^{1/2} = 0.16$ °C. This translates into a 3σ position error uncertainty of $\delta p_T = 0.16$ pixels. Superposed on

the correlation between position offset and temperature at short time scales, there are temperature variations at longer time scales due to changes in illumination.

There are several factors likely contributing to this remaining temperature dependence. First, the T_{mag} sensor is glued onto the magnet and might therefore only report a proxy for the actual magnet temperature. Second, the magnet temperature can be non-uniform so that there is no unique T_{mag}, especially because the Sm-Co alloy has a specific heat capacity typical of metals (on the order of 400 J/kg °C; compare to 900 J/kg °C for Al) but a thermal conductivity that is significantly lower than that of other metals (around 12 W/m °C; compare with 220 W/m °C for Al). Temperature equilibrium is therefore more difficult to reach. Finally, there may be temperature effects in the electromagnetic elements as well, such as the zoom optics.

2.4. Electric fields

The acceleration voltage is chosen so as to guide (hypothetical) ions with the commanded mass-over-charge onto the center pixel, thereby attempting to compensate for the magnet strength variability. However, the precision with which the electric fields in the instrument can be set is finite, with a 14-bit power supply providing the acceleration voltage, a 12-bit power supply for the transfer optics, an 18-bit supply for the electrostatic analyzer voltages to allow for an accurate temperature compensation, and two 14-bit power supplies for the zoom system [1]. The 14-bit precision for the acceleration potential (which varies over almost 2 decades) leads to discretization intervals of $2\delta V_{accel}/V_{accel} \approx 10^{2/2^{14}} - 1 = 3 \times 10^{-4}$ (for logarithmically spaced potentials). Since $V_{accel} \propto (m_c/z)^{-1}$, the relative error on the mass scale is the same. This translates into discrete steps of $\delta p = \alpha 2\delta(m/z)/(m/z) = \sim 9$ pixels each time V_{accel} changes to account for varying T_{mag}. Ideally, the 18-bit electrostatic analyzer potentials compensate for these steps. The electric field E_{EA} in the analyzer (proportional to the difference between the inner and outer electrostatic analyzer potentials) can be set over a range of about 2 decades with a discretization step of at most $2\delta E_{EA}/E_{EA} \approx 10^{2/2^{18}} = 1.8 \times 10^{-5}$ (logarithmic spacing). The curvature radius in the analyzer is $r \propto 1/E_{EA}$. Therefore, $\delta r/r = \delta E_{EA}/E_{EA}$. This implies $\delta p_E = \alpha \delta E_{EA}/E_{EA} = 0.29$ pixel, corresponding to jumps of 0.58 pixels, which must be considered a lower bound for the 3σ error. As a consequence, there will always remain some jitter in the peak positions.

2.5. Mechanical effects

Strong thermal gradients may exist across the optical tube despite the encapsulation in thermal blankets. Knowing that the primary structure is made of Ti [1] with a thermal expansion coefficient around $\epsilon = 8 \times 10^{-6}$ /°C and assuming a temperature difference of $\Delta T = 50$ °C across the analyzer section with an effective length of $L = 25$ cm and width $W = 12.5$ cm, the resulting tube deformation is $\Delta x \approx \epsilon \Delta T L^2/W = 250$ μm in the direction of the mass dispersion, equivalent to 10 pixels. In reality there may not only be a deformation of the tube that positions the detector in the ion beam, but also the mounting of the zoom optics and other elements may be affected by temperature. Such thermal deformations may lead to stick–slip behavior, i.e., discontinuous changes showing an unpredictable hysteresis effect with temperature.

Another mechanical effect is the misalignment of the ion optics, responsible for the slight offset between mass peak positions on channels A and B [7]. Asymmetric illumination can lead to a torsional deformation of the tube so that this misalignment and thus Δp_{AB} may change with temperature.

2.6. Effects in the ion source

Cometary dust particles occasionally have entered the ion source, leading to interesting signatures [12,15]. Refractory dust material may cover part of the slit. The slit used in high-resolution mode has a width of 14 μm, in the typical size range of cometary dust particles. The prime effect of such dust particles covering part of the slit is a reduction in the instrument transmission. A secondary effect, however, can be a displacement of the mass peak, an effect that does not necessarily must be the same over the entire anode row. If such refractory particles can charge electrostatically, deflection of the ions near the slit may produce unexpected effects.

3. Methodology

This section presents the methodology used to compute the mass calibration relation.

3.1. Form of the mass calibration relation

A basic technique for computing the mass calibration was put forward in [9]. The idea there was simply to use the position of the well-defined and isolated CO_2^+ peak at $m_c/z = 44$ [16] as it varies over time. This was then assumed to represent the variations in position also at other m_c/z. Here, this idea is expanded on and combined with the mass calibration relation of Eq. (2).

A first ingredient for an improved mass calibration is the inclusion of temperature dependence to capture short-term variations in peak position, in the form

$$\Delta p_T(T_{\mathrm{mag}}(t), T_{\mathrm{LEDA}}(t), T_{\mathrm{is}}(t)) =$$
$$\gamma_{\mathrm{mag}}[T_{\mathrm{mag}}(t) - T_{\mathrm{ref}}] + \gamma_{\mathrm{LEDA}}[T_{\mathrm{LEDA}}(t) - T_{\mathrm{ref}}] \tag{7}$$
$$+\gamma_{\mathrm{is}}[T_{\mathrm{is}}(t) - T_{\mathrm{ref}}],$$

with reference temperature $T_{\mathrm{ref}} = 0\,°C$ and proportionality factors γ_{mag}, γ_{LEDA}, and γ_{is}. The rationale is that T_{mag}, T_{LEDA}, and T_{is} represent the different sections of the optical tube, so that this combination captures the linear temperature dependencies completely. Any other short- or long-term variations due to mechanical effects or changing temperatures elsewhere in the instrument are captured by a function of time $D(t)$ that does not depend on m_c/z.

A second ingredient is the possibility that the commanded mass-over-charge position on the detector may depend on m_c/z (instead of being exactly at the center), approximated here by a polynomial of order n,

$$\Delta p_0(m_c/z) = a_1 \frac{m_c/z - m_{\mathrm{ref}}/z}{m_{\mathrm{ref}}/z} + \cdots + a_n \left(\frac{m_c/z - m_{\mathrm{ref}}/z}{m_{\mathrm{ref}}/z} \right)^n, \tag{8}$$

with reference mass-over-charge $m_{\mathrm{ref}}/z = 32$. The assumption that variations with m_c/z are smooth stems from the logic that the entire instrument is controlled by electric potentials that depend on m_c/z. As the electric potentials are discrete, there may be (small) additional corrections $\Delta p_{m_c/z}$ at each m_c/z.

A third ingredient is the fact that Δp_{AB} changes slightly with m_c/z. Therefore, reliable measurements of Δp_{AB} are identified first (for peaks with sufficiently high ion counts, spread over the entire mass range). The value of Δp_{AB} for other m_c/z is obtained by linear interpolation (first in time, then in m_c/z).

This leads to mass calibration relations that are an extension of Eq. (2), giving the position of m/z as a function of time as

$$\hat{p}_A(m/z, t) = p_0 + \alpha(m_c/z) \log \frac{m/z}{m_c/z} + \Delta p_0(m_c/z) + \Delta p_{m_c/z}$$
$$+ \Delta p_T(t) + \frac{1}{2}\Delta p_{AB}(t, m_c/z) + D(t), \tag{9}$$
$$\hat{p}_B(m/z, t) = p_0 + \alpha(m_c/z) \log \frac{m/z}{m_c/z} + \Delta p_0(m_c/z) + \Delta p_{m_c/z}$$

$$+ \Delta p_T(t) - \frac{1}{2}\Delta p_{AB}(t, m_c/z) + D(t), \tag{10}$$

where m_c/z is the commanded mass-over-charge for the peak of mass m/z (the nearest integer mass-over-charge). Note that $\Delta p_0(m_{\mathrm{ref}}/z) = 0$ and $\Delta p_T(T_{\mathrm{ref}}, T_{\mathrm{ref}}, T_{\mathrm{ref}}) = 0$ define the time average of $D(t)$. The dispersion factor $\alpha(m_c/z)$ is given a priori (see Table 1); it is computed for spectra in which multiple well-identified peaks are present and interpolated elsewhere.

3.2. Computational technique

The mass calibration relations of Eq. (9)–(10) contain as unknowns the quantities γ_{mag}, γ_{LEDA}, γ_{is}, $a_1, \ldots, a_n$, $\Delta p_{13}, \ldots, \Delta p_{69}$, and the parameters needed to represent $D(t)$. A multivariate optimization procedure [17,18] is used to find the values that best fit the observations.

The optimization target function compares the observed peak positions to the model positions, i.e., the residuals $r_A = p_A - \hat{p}_A$ and $r_B = p_B - \hat{p}_B$. For any given set of γ_{mag}, γ_{LEDA}, γ_{is}, $a_1, \ldots, a_n$, one can compute

$$P_A(m/z, t) = p_0 + \alpha(m_c/z) \log \frac{m/z}{m_c/z} + \Delta p_0(m_c/z)$$
$$+ \Delta p_T(T_{\mathrm{mag}}) + \frac{1}{2}\Delta p_{AB}(t, m_c/z)$$
$$= \hat{p}_A(m/z, t) - \Delta p_{m_c/z} - D(t), \tag{11}$$
$$P_B(m/z, t) = p_0 + \alpha(m_c/z) \log \frac{m/z}{m_c/z} + \Delta p_0(m_c/z)$$
$$+ \Delta p_T(T_{\mathrm{mag}}) - \frac{1}{2}\Delta p_{AB}(t, m_c/z)$$
$$= \hat{p}_B(m/z, t) - \Delta p_{m_c/z} - D(t). \tag{12}$$

The residuals can then be expressed as

$$r_A = p_A - \hat{p}_A = p_A - [P_A + \Delta p_{m_c/z} + D(t)]$$
$$\approx p_A - [P_A + D(t)] = R_A, \tag{13}$$
$$r_B = p_B - \hat{p}_B = p_B - [P_B + \Delta p_{m_c/z} + D(t)]$$
$$\approx p_B - [P_B + D(t)] = R_B, \tag{14}$$

since the $\Delta p_{m_c/z}$ are only small corrections. Therefore, $D(t)$ can be determined by simultaneously fitting $p_A - P_A$ and $p_B - P_B$ for all the peaks, weighed by the uncertainties of Eq. (3), using a least-squares approach. A piecewise linear spline is used here to represent $D(t)$, regularized by a smoothing factor (which is needed to avoid overfitting and to deal with data gaps). Once $D(t)$ is computed, the model peak positions (without accounting for the $\Delta p_{m_c/z}$) are known and one obtains R_A and R_B. The optimization target function is then formulated as

$$F = \frac{1}{a^2}F_1 + F_2, \tag{15}$$

with

$$F_1 = \frac{1}{2\nu} \sum_{i=1}^{\nu} \left[\left(\frac{\langle R_A \rangle_i}{\mathrm{std}(R_A)_i} \right)^2 + \left(\frac{\langle R_B \rangle_i}{\mathrm{std}(R_B)_i} \right)^2 \right] \tag{16}$$

$$F_2 = \frac{1}{2\nu} \sum_{i=1}^{\nu} \left[\sum_{j=1}^{n_{Ai}} \left(\frac{R_{Aij}}{\delta p_{Aij}} \right)^2 + \sum_{j=1}^{n_{Bi}} \left(\frac{R_{Bij}}{\delta p_{Bij}} \right)^2 \right] \tag{17}$$

where ν is the number of peaks that is considered and n_{Ai} and n_{Bi}, $i = 1 \ldots \nu$, give the number of spectra available for peak i. The F_1 term expresses the offset of the average residuals $\langle R_A \rangle_i$ and $\langle R_B \rangle_i$ for the different species from zero (weighed by the respective standard deviation), while F_2 accounts for the variances of the residuals; the constant $a = 1/20$ indicates how much the residual bias reduction is favored over minimizing the spread of the residuals.

The resulting optimization problem has $3 + n$ unknowns, a small number that, moreover, is independent of the number of ion species considered. Since the optimization problem is nonlinear, the difficulty is to find a good starting solution and to avoid getting trapped in local minima. The following procedure was found to work well.
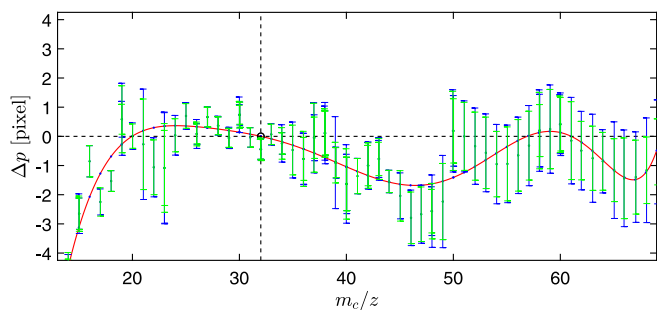
Fig. 6. The red curve gives the continuous variability $\Delta p_0(m_c/z)$ of the peak position offset as a polynomial; the actual peak offsets differ from the continuous curve since they also include a discrete component $\Delta p_{m_c/z}$. The error bars reflect the 1σ variability of the residuals (blue/green for channel A/B), see also Table 3. For $m_c/z = 32$, $\Delta p = 1$ pixel corresponds to $\Delta m/z = 0.001$..

Table 2

Main peak position fit parameter values.

γ_{mag}	1.0419	pixel/°C
γ_{LEDA}	−0.0653	pixel/°C
γ_{is}	−0.1100	pixel/°C
a_1	−2.6257	pixel
a_2	−6.1319	pixel
a_3	−8.8714	pixel
a_4	17.9194	pixel
a_5	95.7488	pixel
a_6	−105.2135	pixel
a_7	−44.7335	pixel
a_8	53.0774	pixel

Phase 1: The problem is solved while using only 1/100th of the number of data points, with a modest precision (a relative precision $\epsilon = 0.0001 a^2$ on the optimization parameters) and a smooth $D(t)$ (only 20 discretization points, smoothing parameter 1), in successive steps. In a first step only $m_c/z = 15$, 20, 30, and 32 are used, benefiting from their well-defined peak positions. In subsequent steps, the set of m_c/z-values is progressively expanded until all values are included, each time improving the previously obtained fit. In the course of this process, the degree of the polynomial is chosen as half the number of m_c/z-values, increasing up to a maximum $n = 8$. At the end of this phase, the solution is further improved by optimizing to a high precision ($\epsilon = 0.0000001 a^2$), using all the data for all m_c/z, but still maintaining a smooth $D(t)$. The data are then filtered to remove data points that are manifest outliers corresponding to peak misidentifications, by requiring the measured peak positions to be within 5 times the standard deviation from the running mean, and in any case not more than 5 pixels off.

Phase 2: The solution is then refined by keeping the obtained temperature dependencies γ_{mag}, γ_{LEDA}, γ_{is}, but using a more accurate representation for $D(t)$ with 10 000 points. In 10 steps the smoothing constant is progressively decreased down to 10^{-14} (computations with low precision, the fraction of data points used is progressively increased from 1/100th to the full set of points). In a last step, the problem is solved to high precision.

Phase 3: After a final outlier removal (again requiring the data points to be within 5 times the standard deviation from the running mean, and not more than 5 pixels off), the problem is solved once more up to high precision.

At the end, the small $\Delta p_{m_c/z}$ corrections are set to the weighted average of the observed deviation for all peaks at m_c/z:

$$\Delta p_{m_c/z} = \frac{\sum_i (\sum_{j=1}^{n_{Ai}} R_{Aij}/\sigma_{Ai} + \sum_{j=1}^{n_{Bi}} R_{Bij}/\sigma_{Bi})}{\sum_i (n_{Ai}/\sigma_{Ai} + n_{Bi}/\sigma_{Bi})}, \tag{18}$$

where i designates the ion species in spectra at m_c/z. If only a single ion species is considered at this m_c/z, if the residual variances on both channels are identical, and if the number of usable spectra on both channels is the same, $n_{Ai} = n_{Bi}$, the deviation is $\Delta p_{m_c/z} = (\langle R_{Ai}\rangle + \langle R_{Bi}\rangle)/2$, the average residual from both channels: The $\Delta p_{m_c/z}$ corrects for the remaining model deviation and thus shifts the residual distribution so that it centers around zero (that would exactly be the case if the average residual would be the same for all species and for both channels).

4. Results and discussion

As a result of the optimization process, the strongest temperature correlation is found to be that with T_{mag}, but smaller correlations with T_{LEDA} and T_{is} contribute as well (Table 2). One can state approximately that the peak position shifts by 1 pixel for every °C of magnet temperature change, in addition to the temperature correction that is already built into the DFMS processing unit (about 16 pixel/°C). The polynomial coefficients a_n are given in Table 2, while Fig. 6 plots the polynomial and shows how $\Delta p_0(m_c/z)$ varies over a few pixels at most, while smaller discrete $\Delta p_{m_c/z}$ are responsible for the deviation of the observed positions. The error bars reflect the 1σ variability of the observed residual distributions. The smooth systematic variation of the peak position offset is largest at low m_c/z, which is where the strongest electric potentials are used in the ion optics. The discrete corrections sometimes show a sharp discontinuity, e.g., between $m/z = 49$ and 50. The error bars are smallest between $m/z = 25$ and 35, where the ion count rates are large so that peak positions are well-defined. Table 3 lists, for each peak, the values of $\Delta p_0(m_c/z)$, $\Delta p_{m_c/z}$, the mean residuals $\langle r_A\rangle$ and $\langle r_B\rangle$, as well as $\text{median}(|r_A|)$ and $\text{median}(|r_B|)$ and the standard deviations $\sigma(r_A)$ and $\sigma(r_B)$. The standard deviations are generally smaller for channel B than for A and are as low as 0.30 pixels for well-defined peaks. This can be compared to the instrumental effects of temperature measurement accuracy and temperature and electric potential discretization, $\delta p_{\text{instr}} = (\delta p_T^2 + \delta p_E^2)^{1/2} = 0.33$ pixel, as a minimum for the 3σ uncertainty. The conclusion is that, for intense peaks, a large fraction of the residual variability can be explained by these instrumental effects. The table also gives the number N_{valid} of valid spectra in which the peak could be visible, i.e., the number of spectra at the corresponding m_c/z after removal of invalid spectra (spectra with data issues or with incompatible information between channel A and B), as well as the number N_{used} of spectra in which the peak was identified and used in the final optimization step. Overall, for a total of about 850 000 mass spectra at 57 different m_c/z, about 705 000 data points have been used from a total of 1 260 000 potential peak positions (56 %) belonging to 84 different fragments. The difference between both is mostly due to peaks that were not intense enough (especially at $m/z = 21$, 23 and > 60), the deformed peaks at 16, 17, 18, and due to failing peak identification. Finally, the time profile $D(t)$ and the observed $\Delta p_{AB}(m_c/z, t)$ profiles are not reported here but can be found in [19].

Fig. 7 presents a visual evaluation of the quality of the fit by displaying both the observed and the model positions. In order to make the figure readable, it focuses on a 10-day interval (1–11 November 2016) and just a few mass peaks. Peak positions are seen to vary during the cold restart after each DFMS shutdown. As temperatures first drop a bit more due to thermal inertia and then recover due to the heat generated by the electronics, the peak positions follow the same trend. The differences between the measured positions (squares/diamonds for channel A/B) and the solid lines (interrupted at data gaps) are small. The same good fitting quality is achieved consistently throughout the entire mission and for all mass peaks (except at $m/z = 16$, 17, and 18 as discussed earlier).

Figs. 8 and 9 show the distribution of r_A for all species considered (plots for r_B are similar). The residuals for well-defined peaks are confined to ± 1.0 pixel ($\sim 3\sigma$), sometimes with half of the distribution within ± 0.2 pixel, the precision down to which the peak position data are given. Less abundant peaks have broader distributions, but still
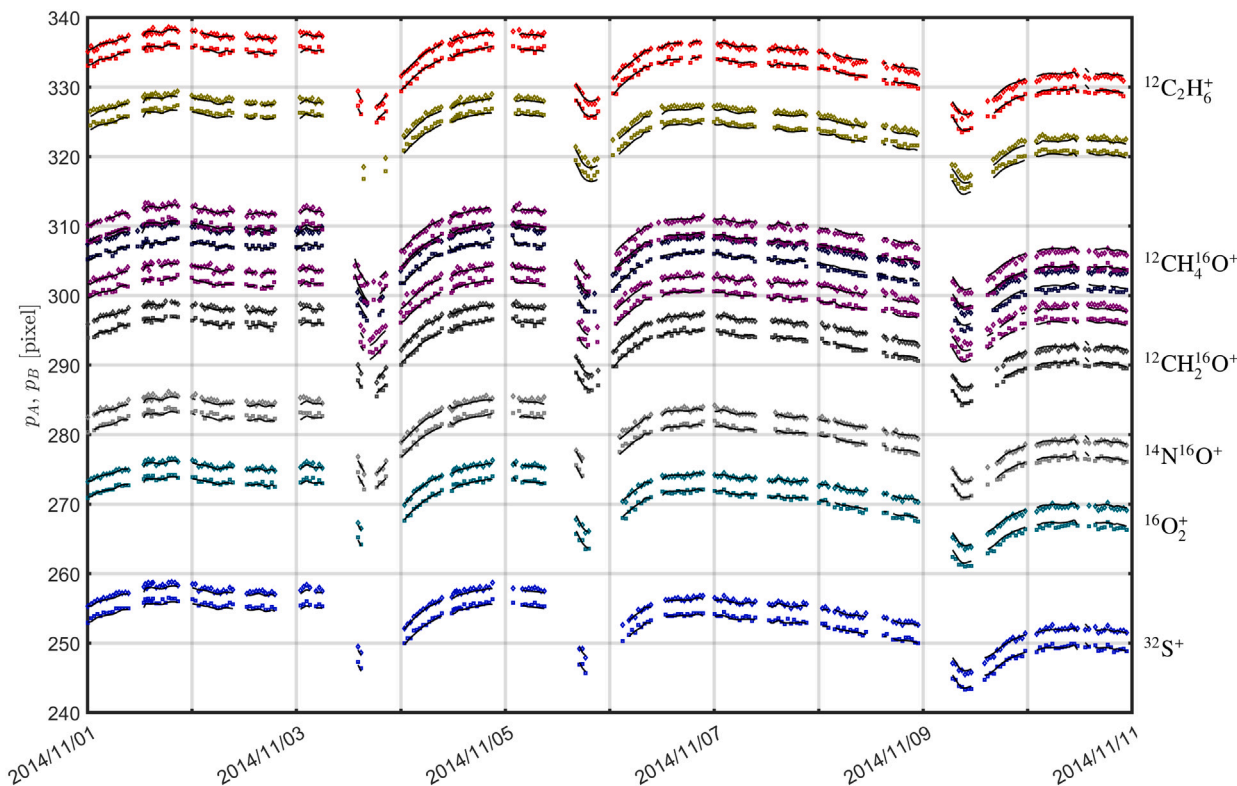
Fig. 7. Observed peak positions p_A (squares) and p_B (diamonds) as well as model positions $\hat{p}_A$ and $\hat{p}_B$ (solid black line segments, interrupted where there are data gaps) for selected species at $m/z = 30$ and 32, during the first days of November 2014.

the bulk of the distribution is within ± 1 pixel. The main reason for this is that the observed peaks are not necessarily at the nominal peak position because of the low count rates and the stochastic nature of the ion detection process [9]. When redoing the analysis with more strict data quality selection and outlier rejection, even smaller distribution widths are found. Among the species considered here, many of the less abundant species are at $m_c/z \geq 50$. At $m/z = 19$, the peaks for $HD^{16}O^+$ and $H_3^{16}O^+$ were deliberately treated as one in the analysis. In the residual distribution, a broad plateau with a width of 2 pixels is found, corresponding to the mass difference between both species. Both species dominate equally often, and sometimes they are both present so that they form a single combined peak at an intermediate mass [see also 20], so this residual behavior is expected. Something similar occurs at $m/z = 21$ for the corresponding species with ^{18}O but with abundances that are much lower. For $^{12}CH^+$ at $m/z = 13$ the fit is poor, which can be ascribed to the rather low count rates and the broadening of the peak due to nearby $^{13}C^+$.

5. Summary and conclusions

In this paper an optimization methodology was described to fit a model of the peak positions observed in DFMS spectra in neutral high resolution modes without post-acceleration. The model takes into account variability due to temperature fluctuations on short time scales (associated with periodic instrument shutdowns) and on long time scales (associated with illumination changes and possibly thermal expansion/contraction). The model is valid for the entire comet encounter. The 1σ-precision is generally better than one pixel.

The T_{mag}-based feedback system implemented in DFMS to account for the change in the strength of the magnet with temperature was able to eliminate $\sim 90\%$ of the corresponding changes in peak position. It could have been advantageous to stabilize the magnet temperature passively (adding thermal insulation, increasing thermal inertia, ...) and/or actively (using heaters), but that would have cost mass and/or

power. In any case, the automatic temperature compensation remains limited by the finite T_{mag} measurement precision. Moreover, in combination with the discretization errors on the electric potentials, the beam positions would still experience a jitter of ~ 0.3 pixel even with a correct temperature compensation system.

Given the consistent good quality of the fit throughout time, for a variety of peaks that appear at different positions on the MCP/LEDA, one can conclude that significant shifts of the peak position because of sharp gradients in MCP gain due to detector aging are absent [7].

Different explanations for the complex time-dependence have been discussed. The small residuals point to a common origin for the time variations captured by γ_{mag}, γ_{LEDA}, γ_{is}, and $D(t)$, regardless of m_c/z. The most likely explanation is that they result from temperature or thermo-mechanical effects and not from electric deviations, since the potential settings are different for the various m_c/z. Also the presence of dust near the slit, immediately downstream of the instrument ion source, may explain part of the time variability.

The DFMS design included a gas calibration unit that provided a few mass reference points at selected m_c/z values. The GCU failed before arrival at the comet. If it would have been available throughout the comet escort phase, it could have been helpful in establishing the mass scale, but because of the finite gas reservoirs and the time needed to perform a GCU calibration run (tens of minutes per run), it could never have resolved the high-frequency time changes in the mass calibration relation. In view of poor pressure regulation by the thermovalves, the use of the GCU for establishing the changes in instrument sensitivity with time would also have been limited.

In conclusion, the physically motivated mass calibration relation presented here consolidates our understanding of DFMS behavior in space. Having an accurate mass calibration is useful for facilitating fragment identification. One of the anticipated uses is in providing the correct common mass scale needed for producing sum spectra, which offer an improved signal-to-noise ratio.
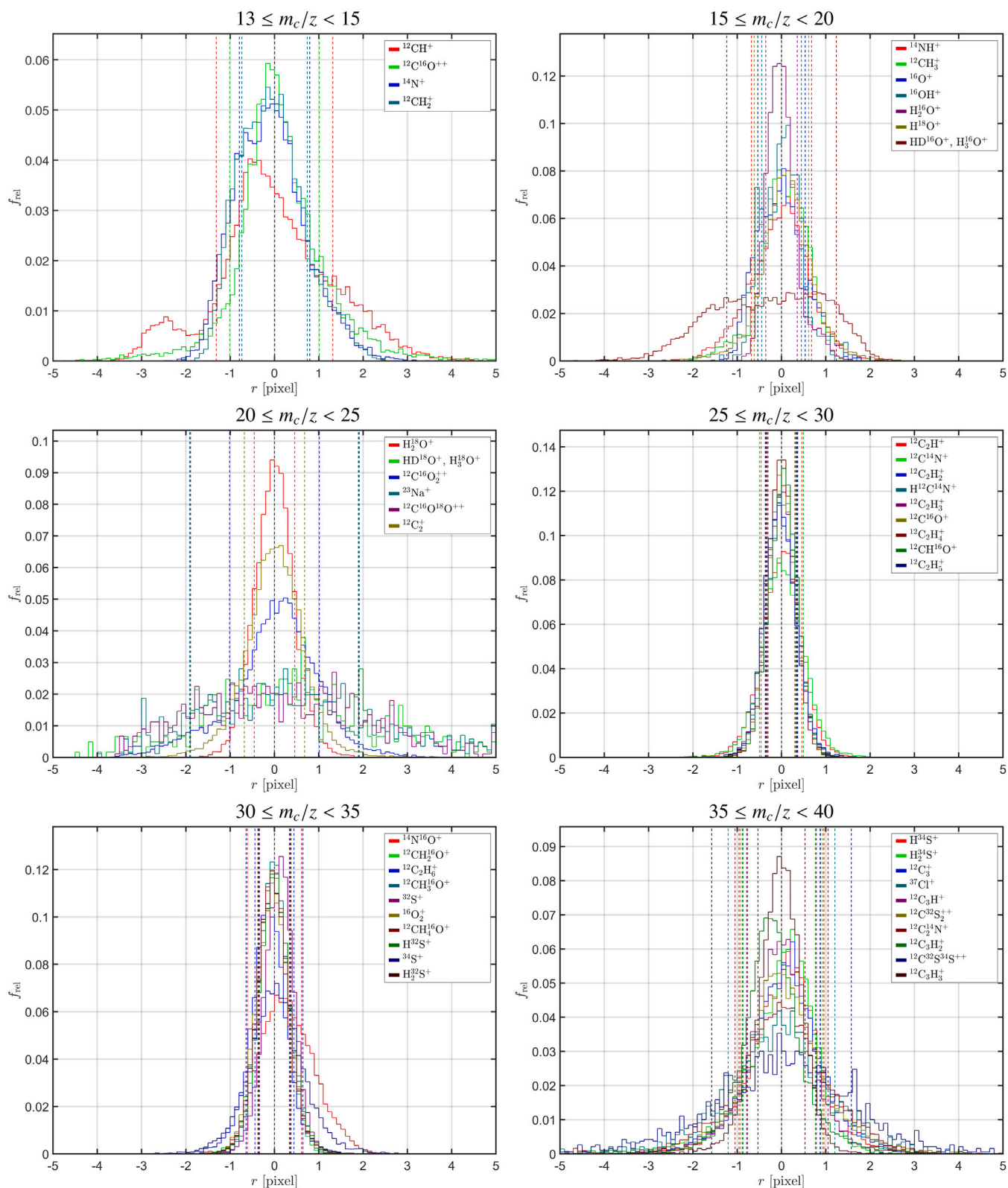
Fig. 8. Distribution of the peak position residuals for all species considered in the fitting procedure at $m/z = 13$–39, for MCP/LEDA channel A. Dashed vertical lines correspond to $\pm\sigma(r_A)$. The distributions typically are confined to $\pm 3\sigma(r_A)$.

While the mass calibration technique described here has been developed specifically for DFMS, it has more general applicability. Any type of mass spectrometer that employs a magnetic field must account for the change of magnetic field strength with temperature. A first approach is to use a thermostat to keep the magnet temperature within a narrow range. Such an approach may be limited by the thermal inertia of the instrument. Also, the operation of heaters might introduce undesirable temperature gradients within the magnet. In the case of mass spectrometers that combine a magnetic and an electric sector, like in the Nier–Johnson setup [5], another way to cope with changing
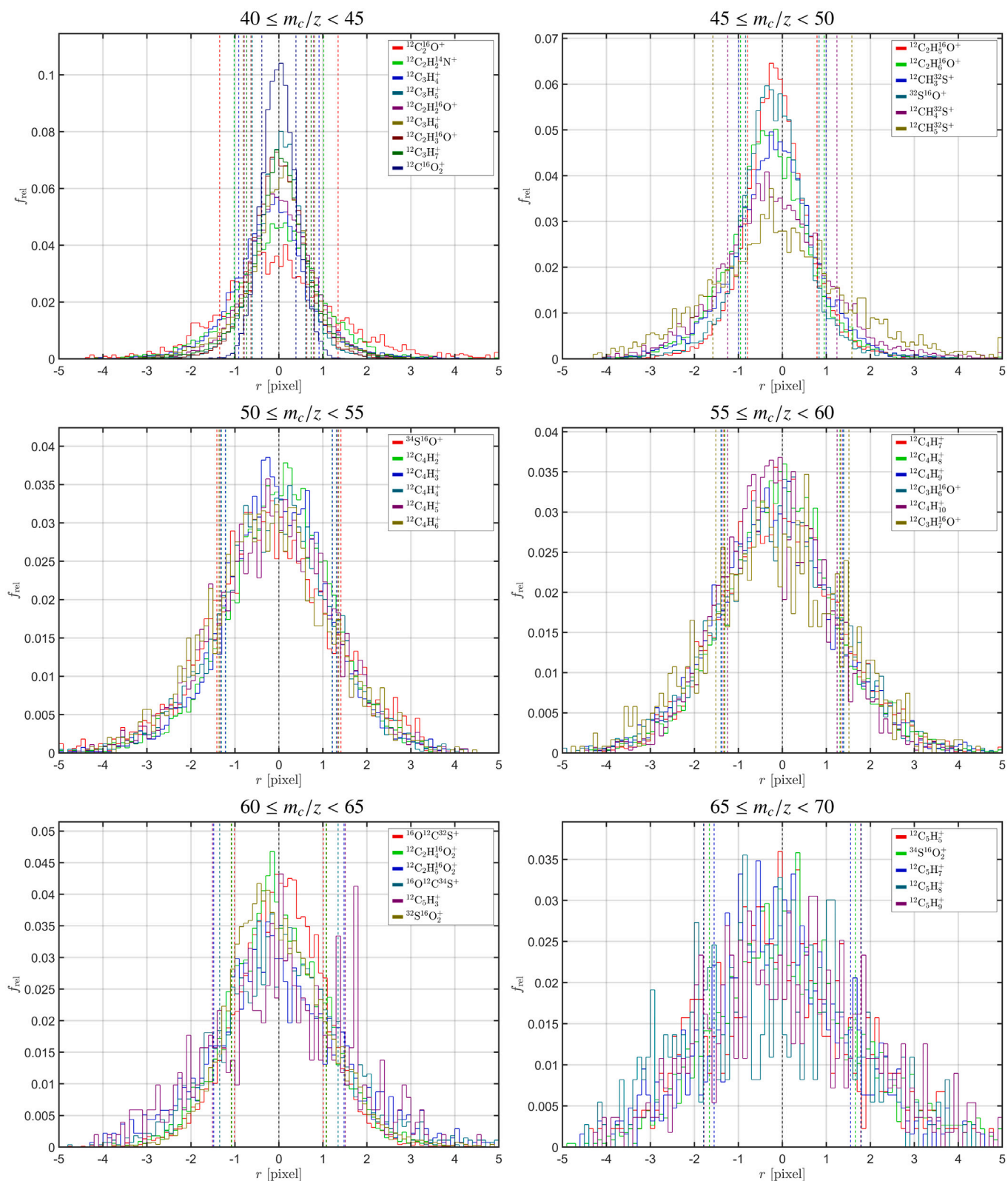
Fig. 9. Distribution of the peak position residuals for all species considered in the fitting procedure at $m/z = 40$–69, for MCP/LEDA channel A. Dashed vertical lines correspond to $\pm\sigma(r_A)$. The distributions typically are confined to $\pm3\sigma(r_A)$.

magnet strength is to compensate for it by adapting the electrostatic potentials in the instrument. However, there are limits on the precision of the magnet temperature measurement that drives this adaptation, and also the discretization of the electric field is a constraint. A third

way to avoid magnet temperature problems is to alternate measurements of the sample with measurements of a reference sample with species at known nearby m/z to provide an experimental calibration. If any of these approaches (or a combination of them) fails to deliver

Table 3

Offsets $\Delta p_0(m_c/z)$ and $\Delta p_{m_c/z}$, A and B residual mean $\langle r \rangle$, median($|r|$) and standard deviation $\sigma(r)$, number of valid spectra N_{valid} and number used N_{used}.

m_c/z	ion	$\Delta p_0(m_c/z)$ [pixel]	$\Delta p_{m_c/z}$ [pixel]	$\langle r_A \rangle$ [pixel]	median($|r_A|$) [pixel]	$\sigma(r_A)$ [pixel]	$\langle r_B \rangle$ [pixel]	median($|r_B|$) [pixel]	$\sigma(r_B)$ [pixel]	N_{valid}	N_{used}
13	$^{12}CH^+$	−6.21	+0.38	0.00	0.77	1.32	0.00	0.77	1.31	15 259	12 789
14	$^{12}C^{16}O^{++}$	−4.49	−0.57	+0.13	0.51	1.01	+0.21	0.63	1.08	15 248	7445
14	$^{14}N^+$	−4.49	−0.57	−0.08	0.55	0.79	−0.07	0.60	0.85	15 248	11 036
14	$^{12}CH_2^+$	−4.49	−0.57	−0.05	0.52	0.74	−0.05	0.50	0.71	15 248	11 993
15	$^{14}NH^+$	−3.12	+0.47	−0.05	0.43	0.68	−0.04	0.39	0.60	15 240	12 901
15	$^{12}CH_3^+$	−3.12	+0.47	+0.04	0.34	0.54	+0.03	0.34	0.54	15 240	12 986
16	$^{16}O^+$	−2.07	+1.22	0.00	0.38	0.53	0.00	0.38	0.54	16 020	3174
17	$^{16}OH^+$	−1.27	−0.97	+0.01	0.30	0.45	−0.01	0.30	0.49	16 030	383
18	$H_2^{16}O^+$	−0.69	−0.84	+0.02	0.21	0.36	−0.02	0.21	0.36	59 469	7771
19	$H^{18}O^+$	−0.27	+0.86	+0.12	0.35	0.61	+0.18	0.36	0.51	16 008	12 517
19	$HD^{16}O^+$, $H_3^{16}O^+$	−0.27	+0.86	−0.30	0.97	1.24	−0.34	0.95	1.15	16 008	12 666
20	$H_2^{18}O^+$	+0.01	−0.00	0.00	0.29	0.46	0.00	0.27	0.42	17 436	14 758
21	$HD^{18}O^+$, $H_3^{18}O^+$	+0.19	−0.46	+0.42	1.33	1.89	−0.34	0.98	1.55	15 993	607
22	$^{12}C^{16}O_2^{++}$	+0.30	−1.36	0.00	0.58	1.01	0.00	0.56	0.94	17 412	12 901
23	$^{23}Na^+$	+0.35	−1.43	+0.35	1.32	1.92	−0.14	0.99	1.52	15 179	856
23	$^{12}C^{16}O^{18}O^{++}$	+0.35	−1.43	+0.22	1.37	1.90	−0.27	0.88	1.29	15 179	891
24	$^{12}C_2^+$	+0.37	−0.33	0.00	0.40	0.68	0.00	0.36	0.57	15 170	12 726
25	$^{12}C_2H^+$	+0.36	+0.34	0.00	0.29	0.46	0.00	0.27	0.42	15 162	12 962
26	$^{12}C^{14}N^+$	+0.33	−0.25	+0.03	0.31	0.50	+0.02	0.27	0.41	15 149	13 102
26	$^{12}C_2H_2^+$	+0.33	−0.25	−0.02	0.24	0.35	−0.01	0.23	0.34	15 149	13 124
27	$H^{12}C^{14}N^+$	+0.29	+0.37	+0.01	0.23	0.35	−0.04	0.22	0.34	15 152	12 953
27	$^{12}C_2H_3^+$	+0.29	+0.37	−0.01	0.23	0.34	+0.04	0.23	0.34	15 152	12 976
28	$^{12}C^{16}O^+$	+0.25	+0.11	0.00	0.21	0.33	−0.04	0.21	0.31	17 517	15 207
28	$^{12}C_2H_4^+$	+0.25	+0.11	0.00	0.20	0.30	+0.05	0.20	0.30	17 517	15 237
29	$^{12}CH^{16}O^+$	+0.20	−0.25	+0.04	0.22	0.33	0.00	0.21	0.32	15 112	12 996
29	$^{12}C_2H_5^+$	+0.20	−0.25	−0.03	0.24	0.37	−0.01	0.22	0.33	15 112	12 976
30	$^{14}N^{16}O^+$	+0.14	+0.60	+0.30	0.43	0.61	+0.22	0.34	0.46	17 511	15 032
30	$^{12}CH_2^{16}O^+$	+0.14	+0.60	−0.05	0.23	0.35	−0.09	0.22	0.33	17 511	15 095
30	$^{12}C_2H_6^+$	+0.14	+0.60	−0.14	0.28	0.44	−0.11	0.25	0.43	17 511	14 929
31	$^{12}CH_3^{16}O^+$	+0.08	−0.11	0.00	0.22	0.34	0.00	0.22	0.33	14 358	12 495
32	$^{32}S^+$	0.00	−0.44	+0.11	0.23	0.34	0.05	0.23	0.35	14 349	12 427
32	$^{16}O_2^+$	0.00	−0.44	−0.05	0.24	0.37	−0.04	0.22	0.34	14 349	12 480
32	$^{12}CH_4^{16}O^+$	0.00	−0.44	−0.04	0.23	0.36	−0.03	0.25	0.39	14 349	12 413
33	$H^{32}S^+$	−0.09	+0.16	0.00	0.23	0.37	0.00	0.22	0.35	14 346	12 392
34	$^{34}S^+$	−0.19	−0.05	+0.04	0.39	0.64	+0.01	0.31	0.54	14 319	11 284
34	$H_2^{32}S^+$	−0.19	−0.05	−0.02	0.23	0.37	−0.01	0.23	0.37	14 319	12 261
35	$H^{34}S^+$	−0.31	−0.16	+0.06	0.51	0.96	−0.05	0.34	0.85	14 320	7849
36	$H_2^{34}S^+$	−0.43	−0.34	−0.07	0.48	0.89	−0.17	0.38	0.95	15 750	6680
36	$^{12}C_3^+$	−0.43	−0.34	+0.07	0.50	0.87	+0.13	0.39	0.74	15 750	7055
37	$^{37}Cl^+$	−0.58	+0.53	−0.11	0.73	1.20	−0.02	0.69	1.18	14 302	1434
37	$^{12}C_3H^+$	−0.58	+0.53	−0.03	0.44	0.79	+0.10	0.39	0.71	14 302	9463
38	$^{12}C^{32}S_2^{++}$	−0.73	+0.84	+0.09	0.52	0.93	+0.13	0.43	0.83	15 745	10 134
38	$^{12}C_2^{14}N^+$	−0.73	+0.84	+0.01	0.65	1.05	+0.07	0.43	0.78	15 745	6158
38	$^{12}C_3H_2^+$	−0.73	+0.84	−0.18	0.44	0.77	−0.09	0.38	0.75	15 745	11 654
39	$^{12}C^{32}S^{34}S^{++}$	−0.88	−0.02	+0.03	0.99	1.58	−0.06	0.36	0.70	14 293	1896
39	$^{12}C_3H_3^+$	−0.88	−0.02	−0.06	0.32	0.53	+0.10	0.30	0.51	14 293	10 036
40	$^{12}C_2^{16}O^+$	−1.04	−0.59	+0.02	0.80	1.35	+0.14	0.73	1.21	15 736	2213
40	$^{12}C_2H_2^{14}N^+$	−1.04	−0.59	0.00	0.61	1.02	+0.10	0.44	0.92	15 736	6539
40	$^{12}C_3H_4^+$	−1.04	−0.59	−0.16	0.51	0.91	−0.05	0.44	0.91	15 736	9120
41	$^{12}C_3H_5^+$	−1.20	−0.17	0.00	0.35	0.61	0.00	0.35	0.60	16 788	14 550
42	$^{12}C_2H_2^{16}O^+$	−1.34	+0.34	+0.01	0.49	0.79	−0.02	0.36	0.69	16 786	14 238
42	$^{12}C_3H_6^+$	−1.34	+0.34	−0.01	0.44	0.81	+0.02	0.41	0.78	16 786	13 863
43	$^{12}C_2H_3^{16}O^+$	−1.47	+0.69	0.00	0.38	0.63	−0.08	0.33	0.57	16 764	14 579
43	$^{12}C_3H_7^+$	−1.47	+0.69	+0.04	0.39	0.73	+0.06	0.37	0.70	16 764	13 761
44	$^{12}C^{16}O_2^+$	−1.57	+0.02	0.00	0.26	0.39	0.00	0.25	0.38	18 380	16 406
45	$^{12}C_2H_5^{16}O^+$	−1.64	−0.40	−0.11	0.46	0.79	+0.12	0.63	0.87	15 223	13 383
46	$^{12}C_2H_6^{16}O^+$	−1.68	−1.11	−0.29	0.60	0.95	+0.27	0.67	0.88	15 206	7795
47	$^{12}CH_3^{32}S^+$	−1.67	−0.99	−0.18	0.59	0.99	+0.17	0.64	0.93	15 203	10 004
48	$^{32}S^{16}O^+$	−1.63	−0.94	−0.20	0.49	0.84	+0.05	0.47	0.75	15 206	10 058
48	$^{12}CH_4^{32}S^+$	−1.63	−0.94	−0.15	0.77	1.24	+0.29	0.62	0.95	15 206	5067
49	$^{12}CH_5^{32}S^+$	−1.54	−0.70	−0.06	0.95	1.58	+0.05	0.86	1.31	15 190	3012
50	$^{34}S^{16}O^+$	−1.41	+1.60	−0.18	0.92	1.41	−0.11	0.89	1.36	15 183	3315
50	$^{12}C_4H_2^+$	−1.41	+1.60	+0.01	0.77	1.21	+0.23	0.79	1.10	15 183	6025
51	$^{12}C_4H_3^+$	−1.24	+1.24	−0.06	0.76	1.21	+0.06	0.79	1.16	10 609	5524
52	$^{12}C_4H_4^+$	−1.04	+0.70	−0.11	0.84	1.31	+0.10	0.78	1.17	10 610	4242
53	$^{12}C_4H_5^+$	−0.82	+0.25	−0.14	0.89	1.33	+0.13	0.82	1.22	10 614	3721
54	$^{12}C_4H_6^+$	−0.59	−0.37	−0.23	0.90	1.36	+0.19	0.73	1.12	10 592	2470
55	$^{12}C_4H_7^+$	−0.36	−0.58	−0.04	0.88	1.33	+0.04	0.81	1.27	10 589	5483
56	$^{12}C_4H_8^+$	−0.15	−0.50	−0.03	0.81	1.31	+0.03	0.80	1.23	10 581	5280
57	$^{12}C_4H_9^+$	+0.01	−0.33	−0.14	0.90	1.37	+0.12	0.76	1.18	10 584	3727
58	$^{12}C_3H_6^{16}O^+$	+0.13	+0.07	−0.10	0.91	1.40	−0.06	0.85	1.31	10 579	3345
58	$^{12}C_4H_{10}^+$	+0.13	+0.07	−0.18	0.83	1.25	+0.23	0.55	0.89	10 579	2825

Table 3 (continued).

m_c/z	ion	$\Delta p_0(m_c/z)$ [pixel]	$\Delta p_{m_c/z}$ [pixel]	$\langle r_A \rangle$ [pixel]	median($|r_A|$) [pixel]	$\sigma(r_A)$ [pixel]	$\langle r_B \rangle$ [pixel]	median($|r_B|$) [pixel]	$\sigma(r_B)$ [pixel]	N_{valid}	N_{used}
59	$^{12}C_3H_7^{16}O^+$	+0.17	+0.08	−0.16	1.04	1.51	+0.14	0.95	1.36	10 574	1210
60	$^{16}O^{12}C^{32}S^+$	+0.13	+0.28	+0.03	0.65	1.01	+0.03	0.63	0.97	10 573	7740
60	$^{12}C_2H_4^{16}O_2^+$	+0.13	+0.28	−0.04	0.71	1.07	−0.01	0.58	0.92	10 573	3378
61	$^{12}C_2H_5^{16}O_2^+$	0.00	−0.15	−0.04	0.94	1.48	+0.04	0.85	1.34	10 576	1375
62	$^{16}O^{12}C^{34}S^+$	−0.21	−0.28	+0.03	0.86	1.35	−0.02	0.63	1.00	10 573	2764
63	$^{12}C_5H_3^+$	−0.50	−0.25	−0.03	1.03	1.51	+0.02	0.77	1.10	11 569	509
64	$^{32}S^{16}O_2^+$	−0.83	−0.02	0.00	0.72	1.08	0.00	0.67	0.99	13 011	9377
65	$^{12}C_5H_5^+$	−1.16	0.00	−0.05	1.09	1.66	+0.03	0.71	1.08	13 005	445
66	$^{34}S^{16}O_2^+$	−1.41	−0.03	+0.12	1.04	1.66	−0.10	0.89	1.38	12 994	2263
67	$^{12}C_5H_7^+$	−1.48	+0.09	−0.11	0.99	1.55	+0.09	0.89	1.27	11 555	632
68	$^{12}C_5H_8^+$	−1.24	+0.07	−0.26	1.29	1.79	+0.17	0.83	1.14	11 978	366
69	$^{12}C_5H_9^+$	−0.49	−0.04	+0.12	1.26	1.78	−0.07	0.76	1.13	10 538	557

a mass scale precision that is comparable to the mass resolution of the instrument, the technique described in this paper can be relevant, at least in situations where continuous measurements are made at different m/z: By identifying the main peaks and following their changing positions over time, the correlation with the temperature of the magnet and/or other parts of the instrument can be determined and the residual time dependence can be fitted in an ad hoc fashion. The usefulness of the approach lies in its being able to provide an accurate mass calibration for past measurements. Extrapolating the calibration to future measurements is only partially possible: One can use the temperature correlation, but the residual time dependence is not known in advance.

CRediT authorship contribution statement

J. De Keyser: Writing – review & editing, Writing – original draft, Visualization, Validation, Supervision, Software, Resources, Project administration, Methodology, Investigation, Funding acquisition, Formal analysis, Data curation, Conceptualization. **F. Dhooghe:** Writing – review & editing, Validation, Data curation. **K. Altwegg:** Writing – review & editing. **M. Rubin:** Writing – review & editing, Visualization, Validation. **N. Hänni:** Writing – review & editing, Visualization, Validation. **S.A. Fuselier:** Writing – review & editing, Resources. **J.-J. Berthelier:** Writing – review & editing, Resources. **E. Neefs:** Writing – review & editing, Resources.

Declaration of competing interest

The authors declare that they have no known competing financial interests or personal relationships that could have appeared to influence the work reported in this paper.

Data availability

The data and software are provided publicly at doi:10.18758/71021093.

References

[1] H. Balsiger, K. Altwegg, P. Bochsler, P. Eberhardt, J. Fischer, S. Graf, A. Jäckel, E. Kopp, U. Langer, M. Mildner, J. Müller, T. Riesen, M. Rubin, S. Scherer, P. Wurz, S. Wüthrich, E. Arijs, S. Delanoye, J. De Keyser, E. Neefs, D. Nevejans, H. Rème, C. Aoustin, C. Mazelle, J.-L. Médale, J.A. Sauvaud, J.-J. Berthelier, J.-L. Bertaux, L. Duvet, J.-M. Illiano, S.A. Fuselier, A.G. Ghielmetti, T. Magoncelli, E.G. Shelley, A. Korth, K. Heerlein, H. Lauche, S. Livi, A. Loose, U. Mall, B. Wilken, F. Gliem, B. Fiethe, T.I. Gombosi, B. Block, G.R. Carignan, L.A. Fisk, J.H. Waite, D.T. Young, H. Wollnik, Rosina - Rosetta Orbiter Spectrometer for Ion and Neutral Analysis, Space Sci. Rev. 128 (1–4) (2007) 745–801, http://dx.doi.org/10.1007/s11214-006-8335-3.

[2] K. Altwegg, H. Balsiger, A. Bar-Nun, J.-J. Berthelier, A. Bieler, P. Bochsler, C. Briois, U. Calmonte, M. Combi, J. De Keyser, P. Eberhardt, B. Fiethe, S.A. Fuselier, S. Gasc, T.I. Gombosi, K.C. Hansen, M. Hässig, A. Jäckel, E. Kopp, A. Korth, L. Le Roy, U. Mall, B. Marty, O. Mousis, E. Neefs, T. Owen, H. Rème, M. Rubin, T. Sémon, C.-Y. Tzou, H. Waite, P. Wurz, 67P/Churyumov-Gerasimenko, a Jupiter family comet with a high D/H ratio, Science 347 (6220) (2014) 1261952, http://dx.doi.org/10.1126/science.1261952.

[3] A. Bieler, K. Altwegg, H. Balsiger, A. Bar-Nun, J.-J. Berthelier, P. Bochsler, C. Briois, U. Calmonte, M. Combi, J. De Keyser, E.F. van Dishoeck, B. Fiethe, S.A. Fuselier, S. Gasc, T.I. Gombosi, K.C. Hansen, M. Hässig, A. Jäckel, E. Kopp, A. Korth, L. Le Roy, U. Mall, R. Maggiolo, B. Marty, O. Mousis, T. Owen, H. Rème, M. Rubin, T. Sémon, C.-Y. Tzou, J.H. Waite, C. Walsh, P. Wurz, Abundant molecular oxygen in the coma of comet 67P/Churyumov-Gerasimenko, J. Inst. Math. Appl. 526 (2015) 678–681, http://dx.doi.org/10.1038/nature15707.

[4] P. Wurz, M. Rubin, K. Altwegg, H. Balsiger, J.-J. Berthelier, A. Bieler, U. Calmonte, J. De Keyser, B. Fiethe, S.A. Fuselier, A. Galli, S. Gasc, T.I. Gombosi, A. Jäckel, L. Le Roy, U. Mall, H. Rème, V. Tenishev, C.-Y. Tzou, Solar wind sputtering of dust on the surface of 67P/Churyumov-Gerasimenko, Astron. Astrophys. 583 (2015) A22, http://dx.doi.org/10.1051/0004-6361/201525980.

[5] E.G. Johnson, A.O. Nier, Angular aberrations in sector shaped electromagnetic lenses for focusing beams of charged particles, Phys. Rev. 91 (1953) 10–17.

[6] J.-J. Berthelier, J.-M. Illiano, D. Nevejans, E. Neefs, E. Arijs, N. Schoon, High resolution focal plane detector for a space-borne magnetic mass spectrometer, Int. J. Mass Spectrom. 215 (1–3) (2002) 89–100, http://dx.doi.org/10.1016/S1387-3806(02)00527-4.

[7] J. De Keyser, K. Altwegg, A. Gibbons, F. Dhooghe, H. Balsiger, J.-J. Berthelier, S. Fuselier, T. Gombosi, E. Neefs, M. Rubin, Position-dependent microchannel plate gain correction in Rosetta's ROSINA/DFMS mass spectrometer, Int. J. Mass Spectrom. 446 (2019) 116232, http://dx.doi.org/10.1016/j.ijms.2019.116232.

[8] D. Nevejans, E. Neefs, S. Kavadias, P. Merken, C. Van Hoof, The LEDA512 integrated circuit anode array for the analog recording of mass spectra, Int. J. Mass Spectrom. 215 (1) (2002) 77–87, http://dx.doi.org/10.1016/S1387-3806(01)00549-8.

[9] J. De Keyser, A. Gibbons, F. Dhooghe, K. Altwegg, H. Balsiger, J.-J. Berthelier, S. Fuselier, T. Gombosi, E. Neefs, M. Rubin, Calibration of parent and fragment ion detection rates in Rosetta's ROSINA/DFMS mass spectrometer, Int. J. Mass Spectrom. 446 (2019) 116233, http://dx.doi.org/10.1016/j.ijms.2019.116233.

[10] J. De Keyser, F. Dhooghe, A. Gibbons, K. Altwegg, H. Balsiger, J.-J. Berthelier, C. Briois, U. Calmonte, G. Cessateur, E. Equeter, B. Fiethe, S.A. Fuselier, T. Gombosi, H. Gunell, M. Hässig, L. Le Roy, R. Maggiolo, E. Neefs, M. Rubin, T. Sémon, Correcting peak deformation in Rosetta's ROSINA/DFMS mass spectrometer, Int. J. Mass Spectrom. 393 (2015) 41–51, http://dx.doi.org/10.1016/j.ijms.2015.10.010.

[11] L. Le Roy, K. Altwegg, H. Balsiger, J.-J. Berthelier, A. Bieler, C. Briois, U. Calmonte, M. Combi, J. De Keyser, F. Dhooghe, B. Fiethe, S.A. Fuselier, S.

Gasc, T.I. Gombosi, M. Hässig, A. Jäckel, M. Rubin, C.-Y. Tzou, The volatile inventory of comet 67P/Churyumov-Gerasimenko from Rosetta/ROSINA, Astron. Astrophys. 583 (2015) A1, http://dx.doi.org/10.1051/0004-6361/201526450.

[12] K. Altwegg, H. Balsiger, N. Hänni, et al., Evidence of ammonium salts in comet 67P as explanation for the nitrogen depletion in cometary comae, Nat. Astron. 4 (2020) 533–540, http://dx.doi.org/10.1038/s41550-019-0991-9.

[13] B. Schläppi, K. Altwegg, H. Balsiger, M. Hässig, A. Jäckel, P. Wurz, B. Fiethe, M. Rubin, S.A. Fuselier, J.-J. Berthelier, J. De Keyser, H. Rème, U. Mall, The influence of spacecraft outgassing on the exploration of tenuous atmospheres with in situ mass spectrometry, J. Geophys. Res. 115 (2010) A12313, http://dx.doi.org/10.1029/2010JA015734.

[14] M. Hässig, Sensitivity and fragmentation calibration of the ROSINA Double Focusing Mass Spectrometer (Ph.D. thesis), Universität Bern, 2013.

[15] K. Altwegg, M. Combi, S.A. Fuselier, N. Hänni, J. De Keyser, A. Mahjoub, D.R. Müller, B. Pestoni, M. Rubin, S.F. Wampfler, Abundant ammonium hydrosulphide embedded in cometary dust grains, Mon. Not. R. Astron. Soc. 516 (2022) 3900–3910, http://dx.doi.org/10.1093/mnras/stac2440.

[16] M. Hässig, K. Altwegg, H. Balsiger, A. Bar-Nun, J.-J. Berthelier, A. Bieler, P. Bochsler, C. Briois, U. Calmonte, M. Combi, J. De Keyser, P. Eberhardt, B. Fiethe, S.A. Fuselier, M. Galand, S. Gasc, T.I. Gombosi, K.C. Hansen, A. Jäckel, H.U. Keller, E. Kopp, A. Korth, E. Kührt, L. LeRoy, U. Mall, B. Marty, O. Mousis, E. Neefs, T. Owen, H. Rème, M. Rubin, T. Sémon, C. Tornov, C.-Y. Tzou, H. Waite, P. Wurz, Time variability and heterogeneity in the coma of 67P/Churyumov-Gerasimenko, Science 347 (6220) (2015) aaa0276, http://dx.doi.org/10.1126/science.aaa0276.

[17] C.G. Broyden, The convergence of a class of double-rank minimization algorithms, J. Inst. Math. Appl. 6 (1) (1970) 76–90, http://dx.doi.org/10.1093/imamat/6.1.76.

[18] R. Fletcher, A New Approach to Variable Metric Algorithms, Comput. J. 13 (3) (1970) 317–322, http://dx.doi.org/10.1093/comjnl/13.3.317.

[19] J. De Keyser, Mass calibration of Rosetta's ROSINA/DFMS Mass Spectrometer: Supplementary Materials, Royal Belgian Institute for Space Aeronomy, 2024, http://dx.doi.org/10.18758/71021093.

[20] D. Müller, K. Altwegg, J.-J. Berthelier, M. Combi, J. De Keyser, S.A. Fuselier, N. Hänni, B. Pestoni, M. Rubin, I.R.H.G. Schroeder, S.F. Wampfler, High D/H ratios in water and alkanes in comet 67P/Churyumov-Gerasimenko measured with Rosetta/ROSINA DFMS, Astron. Astrophys. 662 (2022) A69, http://dx.doi.org/10.1051/0004-6361/202142922.